Available online at www.sciencedirect.com
ScienceDirect
Ceramics International 37 (2011) 493–504
CERAMICS INTERNATIONAL
www.elsevier.com/locate/ceramint

Solid solutions of mixed metal $Mn_{3-x}Mg_xFe_4(PO_4)_6$ orthophosphates: Colouring performance within a double-firing ceramic glaze

M. Llusar *, J.A. Badenes, A. García, C. Gargori, R. Galindo, G. Monrós

Departamento de Química Inorgánica y Orgánica, Universitat Jaume I, Edifici Científico-Tècnic, Av. Sos Baynat s/n, 12071 Castellón, Spain

Received 22 July 2010; received in revised form 2 August 2010; accepted 7 September 2010
Available online 25 September 2010

Abstract

Solid solutions of mixed metal $Mn_{3-x}Mg_xFe_4(PO_4)_6$ orthophosphates ($x = 0$, 0.5, 1, 1.5, 2, 2.5, and 3) were prepared for the first time (from coprecipitate powders calcined up to 1000 °C) and characterized by thermal analysis, XRD, SEM/EDX, UV–vis–NIR spectroscopy and colour measurements (CIE-$L^*a^*b^*$). Orthophosphate $(Mn,Mg)_{3-y}Fe_{4+z}(PO_4)_6$ solid solutions isotypic to $Fe_7(PO_4)_6$ structure (triclinic P-1(2) spatial group) formed successfully as the major crystalline phase within the studied range of compositions, accompanied only by variable quantities of α- and/or β-$Mg_2P_2O_7$ diphosphates as secondary phases. Noteworthy, the obtained solid solutions were tested as potential ceramic dyes and exhibited an interesting interaction upon enamelling within a double-firing ceramic glaze: considerable amounts of Fe segregated from the solid solutions to be stabilized as hematite particles (α-Fe_2O_3) in the ceramic glaze and conferring the glaze an intense dark-brown colouration, which was almost independent of the amount of Mg doping. Thus, the obtained solid solutions with a minimized Mn content (especially $Mg_3Fe_4(PO_4)_6$ composition, without Mn) could serve as low-toxicity Fe reservoirs to stabilize hematite in double-firing glazes and produce an interesting dark-brown colouration, being an alternative to other brown ceramic pigments containing hazardous metals (i.e. Cr, Ni, Zn, or Sb).

Keywords: A. Sol–gel processes; C. Colour; Orthophosphates; Hematite; Brown ceramic dyes

1. Introduction

Some recent research on metallic phosphates within the field of ceramic materials have been directed to the development of ceramic pigments or dyes [1–4] and also to obtain new photoluminescent materials [5]. Metallic phosphates are also being profusely investigated for many other advanced applications (such as catalysts, dielectrics, thermo-resistant materials, molecular sieves, sensors, electrochemistry, magnetic and biocompatible materials, etc.) [6–11].

With the scope of obtaining new low-toxicity ceramic pigments [12–15], we have recently investigated some phosphate-based pigments or dyes [3,4,16]. In these previous works, violet-blue ceramic pigments (dyes) were prepared from coprecipitate powders in the solid solution systems of Fe ($FePO_4$) and Co ($Co_3(PO_4)_2$) phosphates [3] and Fe and Co oxy-phosphates ($CoFeOPO_4$) [4], and also in the diphosphate $Co_{2-x}Mg_xP_2O_7$ solid solution system [16]. In these studies, the cobalt content in the obtained solid solutions was minimized as a response to environmental or toxicity concerns [12]. On the other hand, preliminary investigations with $Mn_3Fe_4(PO_4)_6$ phosphates (structure type of $Fe_7(PO_4)_6$) have shown that these systems can produce also interesting brown colourations in ceramic glazes.

The crystalline structure of the mixed-valent iron(II/III) phosphate, $Fe_7(PO_4)_6$ has been described in many studies [17–21] since the first report of Gorbunov et al. [22] existing a large number of isotypic compounds with the general formula $M^{II}_3M^{III}_4(XO_4)_6$ (where M = first row transition metal, and X = P, V, As or Mo) [23–28]. The structure belongs to the triclinic P-1(2) spatial group and contains four independent cation sites: octahedral $M(1)O_6$, $M(2)O_6$, and $M(4)O_6$, and trigonal bipyramid $M(3)O_5$. In the idealized structure the M(1) and M(3) sites are occupied by bivalent cations and the M(2) and M(4) sites are occupied by trivalent cations [19,23], although disordering of bi- and trivalent cations over the M(1) and M(2) sites was observed for some structures (such as $Cu_3Cr_4(PO_4)_6$) [19].

---

* Corresponding author. Tel.: +34 964 728244; fax: +34 964 728214.
E-mail address: mllusar@qio.uji.es (M. Llusar).

0272-8842/$36.00 © 2010 Elsevier Ltd and Techna Group S.r.l. All rights reserved.
doi:10.1016/j.ceramint.2010.09.004

With the above considerations the aim of the present work is the preparation for the first time of solid solutions of mixed metal $Mn_{3-x}Mg_xFe_4(PO_4)_6$ ($x = 0$–3) orthophosphates ($Fe_7(PO_4)_6$ structure type) from coprecipitate powders, and to test their potential use as ceramic dyes for the colouration of low-temperature (1000 °C) ceramic glazes. The replacement of Mn after Mg in the structure is justified attending to environmental or toxicity concerns, since salts and solutions containing heavy metals are considered as potentially hazardous (code 06 03 13) in the European Waste Catalogue (EWC) [29].

The formation of the solid solutions has been characterized by XRD measurements (including cell parameters calculation) and SEM–EDX techniques. On the other hand, the optical and colour properties of the fired powders and enamelled samples (within a conventional double-firing ceramic glaze) have been studied by UV–vis–NIR spectroscopy and CIE-$L^*a^*b^*$ colour measurements. The possible reaction or interaction of the phosphate solid solutions within the ceramic glaze has been also analyzed to determine the origin of the colour in the ceramic glaze.

2. Experimental procedure

2.1. Sample preparation

Solid solutions of mixed metal orthophosphates with compositions $Mn_{3-x}Mg_xFe_4(PO_4)_6$ ($x = 0$, 0.5, 1, 1.5, 2, 2.5, and 3) were prepared through the conventional coprecipitation route, using $Mn(NO_3)_2 \cdot 4H_2O$ (97%, Aldrich), $Mg(NO_3)_2 \cdot 6H_2O$ (99%, Aldrich), $Fe(NO_3)_3 \cdot 9H_2O$ (98%, Aldrich) and H_3PO_4 (80%, Fluka) as precursors. Table 1 indicates the nomenclature used for the prepared initial formulations. In a typical preparation, Mn, Mg and Fe salts were added (in this order) to an aqueous solution (150 mL) containing the required stoichiometric amount of H_3PO_4 (continuously stirred and at room temperature). Aqueous ammonia ($NH_3:H_2O = 1:1$) was then added dropwise to the homogeneous solution until reaching a pH of *ca.* 7–8. The obtained coprecipitate powders were then dried overnight in an electrical dryer (at 110 °C), and the resulting dried powders were subsequently submitted to calcination in an electrical furnace up to 800° and 1000 °C (5 °C/min of heating gradient) with 2 h and 4 h of soaking time at the maximum temperature, respectively.

Table 1
Nomenclature of the theoretical (initial) formulations $Mn_{3-x}Mg_xFe_4(PO_4)_6$ prepared by the coprecipitation route.

Sample	Theoretical formulation
D1 ($x = 0$)	$Mn_3Fe_4(PO_4)_6$
D2 ($x = 0.5$)	$Mn_{2.5}Mg_{0.5}Fe_4(PO_4)_6$
D3 ($x = 1$)	$Mn_2Mg_1Fe_4(PO_4)_6$
D4 ($x = 1.5$)	$Mn_{1.5}Mg_{1.5}Fe_4(PO_4)_6$
D5 ($x = 2$)	$Mn_1Mg_2Fe_4(PO_4)_6$
D6 ($x = 2.5$)	$Mn_{0.5}Mg_{2.5}Fe_4(PO_4)_6$
D7 ($x = 3$)	$Mg_3Fe_4(PO_4)_6$

2.2. Sample characterization

Simultaneous differential thermal and thermo-gravimetric analysis (DTA–TGA) of selected dried coprecipitates was carried out with a Mettler Toledo thermal analyzer (using alumina crucibles with a constant 5 °C/min heating from 50° up to 1250 °C, under air conditions). Crystallochemical characterization of calcined samples was performed by X-ray diffraction (XRD) in a Siemens D-500 Powder Diffractometer with CuK_α radiation (from 15 to 60° 2θ, with steps of 0.02° 2θ; the counting time was of 2 s and 10 s per step for samples calcined at 800° and 1000 °C, respectively). The diffractometer was equipped with a graphite secondary monochromator to eliminate the K_β and fluorescence signals (important in compositions with a large amount of Fe and Mn). Moreover, the cell parameters of 1000 °C-fired solid solutions were also calculated with the *TOPAS* fitting program [30,31] using refined XRD patterns.

On the other hand, the morphology and microstructure of $Mn_{3-x}Mg_xFe_4(PO_4)_6$ solid solutions obtained after calcination at 1000 °C was examined by scanning electron microscopy (SEM) with a Leo-440i Leyca electron microscope (following conventional preparation and imaging techniques). The composition and chemical homogeneity of the samples (Mn:Mg:Fe:P ratio) was determined by semi-quantitative elemental analysis with an EDX analyzer (supplied by Oxford University) attached to the microscope.

In order to analyze the interaction, stability and optical or colouring properties of the obtained solid solutions within a conventional ceramic glaze, the 1000 °C-fired powders were also 5 wt % enamelled within a commercial double-firing transparent glaze (SiO_2–Al_2O_3–PbO–CaO–Na_2O–K_2O system) onto conventional ceramic biscuits, and fired following a fast-firing scheme (52 min of duration from cool to cool at a maximum temperature of 1000 °C). The optical properties of fired powders and enamelled samples were then analyzed by diffuse reflectance spectroscopy (UV–vis–NIR) performed with a Perkin-Elmer (lambda 2000) spectrophotometer. $L^*a^*b^*$ colour parameters were measured using a standard lighting C, following the CIE-$L^*a^*b^*$ colourimetric method recommended by the CIE (Commission Internationale de l'Eclairage) [32]. On this method, L^* is the lightness axis (black (0) → white (100)), b^* is the blue (–) → yellow (+) axis, and a^* is the green (−) → red (+) axis. In addition, the possible interaction of solid solution particles within the glassy matrix was analyzed through SEM observations and EDX measurements, and also by performing X-ray diffraction measurements (grazing angle technique, with 0.05° 2θ per step and 6 s of counting time) onto the surface of enamelled samples.

3. Results and discussion

3.1. Thermal analysis (DTA–TGA)

The differential thermal (DTA) and thermogravimetric (TGA) analyses of two representative $Mn_{3-x}Mg_xFe_4(PO_4)_6$

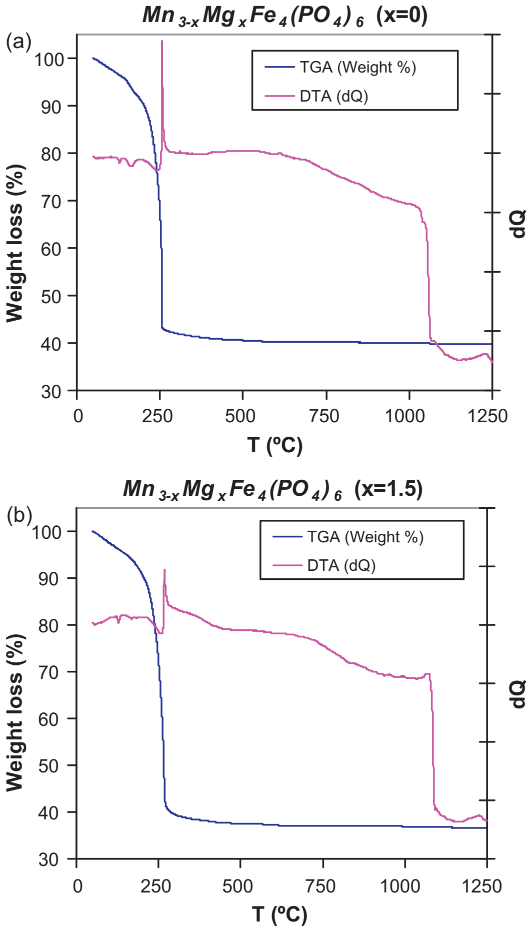

Fig. 1. DTA–TG curves of selected $Mn_{3-x}Mg_xFe_4(PO_4)_6$ samples: (a) $x = 0$, and (b) $x = 1.5$.

coprecipitate powders ($x = 0$ and 1.5) are shown in Fig. 1. In general terms all the thermal analyses show similar features. First some weak endothermic signals around 132–179 °C may be observed (with an associated weight loss of 5–7% in the TGA curve) due to the elimination of water, followed by a sharp exothermic signal around 256–268 °C (with a weight loss of *ca.* 50.4–55.5%), which corresponds to the decomposition of the NH_4NO_3 present in the coprecipitate powders. The last and intense endothermic band occurring at higher temperatures (centred at around 1154–1160 °C) would correspond to the melting of the orthophosphates. Interestingly, the starting temperature for the melting process is shifted to higher temperatures with the increase of Mg doping (x) in the solid solution: 1037 °C for $x = 0$, 1076 °C for $x = 1.5$, and 1105 °C for $x = 3$ (not shown).

3.2. X-ray diffraction characterization (XRD)

The major and secondary crystalline phases present in the XRD patterns of raw and fired samples (800° and 1000 °C) are summarized in Table 2. The XRD patterns of raw samples (not shown) indicate for all the compositions the presence of ammonium nitrate (NH_4NO_3) and also ammonium metallophosphates ($NH_4MPO_4 \cdot H_2O$, with M = Fe, Mn and/or Mg), resulting from the followed coprecipitation route. The XRD patterns of two representative compositions fired at 800 °C/2 h may be seen in Fig. 2. Noteworthy, intense XRD peaks associated to the presence of the $Mn_{3-x}Mg_xFe_4(PO_4)_6$ solid solution phase may be already observed (labelled as P in Fig. 2 and Table 2) at this temperature (800 °C). The position and intensity of the XRD peaks of the formed solid solutions correlate well with those of the isotypic structure $Fe_7(PO_4)_6$ (PDF number 049-1088) and to a higher extent with the $Mn_{2.06}Fe_{4.94}(PO_4)_6$ compound (PDF number 080-0761), that crystallizes in the same $Fe_7(PO_4)_6$ structure type.

Besides, peaks of weak to medium intensity of accessory phases containing Mn, Mg and Fe may be also observed at 800 °C: $Mn_2P_4O_{12}$ for $x \leq 0.5$ (PDF number 038-0314, with main peaks at around 14° and 29° 2θ and labelled as M), $Mn_{1.5}Fe_{1.5}(PO_4)_2$ for $x \leq 1$ (PDF number 085-0925) and $Mg_{1.5}Fe_{1.5}(PO_4)_2$ for $1.5 \leq x \leq 3$ (PDF number 083-1859), both of them with the main XRD peak at around 25.6°2θ (and labelled as P′) and also β-$Mg_2P_2O_7$ for $x \geq 1$ (PDF number 073-0535, with main peaks at around 29.5° and 30.7° 2θ and labelled as β). The presence of these secondary phases of Mn and Mg indicates that the formed solid solutions should contain a smaller quantity of Mn + Mg (<3), or an excess of Fe (>4) with respect to the theoretical $Mn_{3-x}Mg_xFe_4(PO_4)_6$ formulations (this will be later confirmed in the SEM–EDX analyses), as it occurs in the already known $Mn_{2.06}Fe_{4.94}(PO_4)_6$

Table 2
General evolution of crystalline phases (XRD) with the firing temperature for prepared samples with nominal composition $Mn_{3-x}Mg_xFe_4(PO_4)_6$.

Samples	Crystalline samples	Intensity[a]	Composition
Raw samples	N: NH_4NO_3	m–s	$0 \leq x \leq 3$
	A: $NH_4MPO_4 \cdot H_2O$ (M = Fe, Mn, Mg)	s	$0 \leq x \leq 3$
800 °C (2 h)	P: $(Mn,Mg)_{3-y}Fe_{4+z}(PO_4)_6$	s	$0 \leq x \leq 3$
	M: $Mn_2P_4O_{12}$	w	$x \leq 0.5$
	P′: $M_{1.5}Fe_{1.5}(PO_4)_2$ (M = Mn, Mg)	w → m	$0 \leq x \leq 3$
	β: β-$Mg_2P_2O_7$	w–m	$x \geq 1$
1000 °C (4 h)	P: $(Mn,Mg)_{3-y}Fe_{4+z}(PO_4)_6$	vs	$0 \leq x \leq 3$
	M: $Mn_2P_4O_{12}$	vw	$x = 0$
	β: β-$Mg_2P_2O_7$	w → m	$x \geq 1$
	α: α-$Mg_2P_2O_7$	vw	$x = 3$

[a] Intensity of the XRD signal: vw (very weak), w (weak), m (medium), s (strong) and vs (very strong).

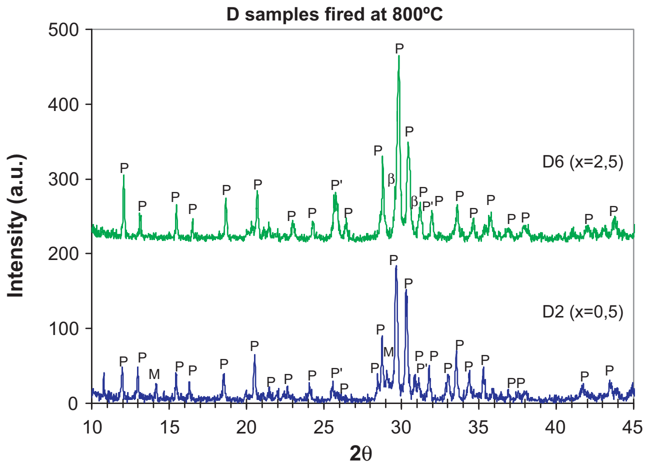

Fig. 2. XRD patterns of representative (selected) $Mn_{3-x}Mg_xFe_4(PO_4)_6$ samples (D2 and D6) fired at 800 °C/2 h. Crystalline phases: P = $(Mn,Mg)_{3-y}Fe_{4+z}(PO_4)_6$, M = $Mn_2P_4O_{12}$, P′ = $M_{1.5}Fe_{1.5}(PO_4)_2$ (with M = Mn, Mg) and β = β-$Mg_2P_2O_7$.

compound. We therefore better refer to the formed solid solutions (P) as $(Mn,Mg)_{3-y}Fe_{4+z}(PO_4)_6$.

On the other hand, the XRD patterns of samples fired at 1000 °C/4 h (see Fig. 3 and Table 2) indicate the formation of well-crystallized $(Mn,Mg)_{3-y}Fe_{4+z}(PO_4)_6$ solid solutions (P) as the major crystalline phase for all the studied compositional range, accompanied by a weak amount of $Mn_2P_4O_{12}$ (only for $x = 0$), increasing amounts of β-$Mg_2P_2O_7$ with the increase of Mg doping (XRD peaks of weak intensity for $1 \leq x < 2$, and of medium intensity for $x \geq 2$), and also a weak amount of α-$Mg_2P_2O_7$ for $x = 3$ (PDF number 072-0019, with main peaks at around 29.7° and 30.1° 2θ and labelled as α).

A clearer evidence of the successful formation of the $Mn_{3-x}Mg_xFe_4(PO_4)_6$ solid solutions was obtained by the calculation of the cell parameters of this major phase. In this respect, Table 3 summarizes the cell parameters (and cell volume) calculated with the TOPAS program from refined XRD patterns [30]. As it may be appreciated (see Fig. 4), there is quite a clear linear tendency in the variation of cell parameters of the $Mn_{3-x}Mg_xFe_4(PO_4)_6$ orthophosphates with the composition (x). The calculated cell parameters (a, b and c) decrease linearly with increasing amounts of Mg (x) in the formulation. As a result, the overall cell volume of the solid solution also diminishes considerably with Mg doping. This is in accordance with the replacement of the larger Mn^{2+} ions (ionic radius = 89 and 97 pm in five-fold and high-spin six-fold coordination, respectively) by the smaller Mg^{2+} ions (ionic radius = 80 and 86 pm in five-fold and six-fold coordination, respectively) [33], in the bivalent cationic sites of the $M^{II}{}_3Fe^{III}{}_4(PO_4)_6$ structure (M(1) octahedral and M(3) trigonal

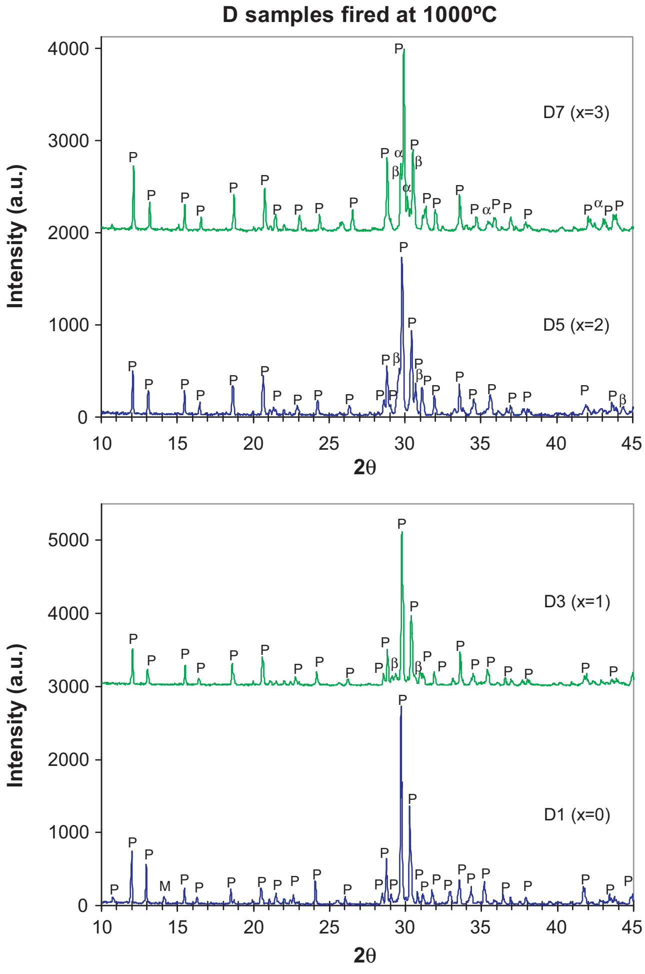

Fig. 3. XRD patterns of representative $Mn_{3-x}Mg_xFe_4(PO_4)_6$ samples (D1, D3, D5 and D7) fired at 1000 °C/4 h. Crystalline phases: P = $(Mn,Mg)_{3-y}Fe_{4+z}(PO_4)_6$, M = $Mn_2P_4O_{12}$, β = β-$Mg_2P_2O_7$ and α = α-$Mg_2P_2O_7$.

Table 3
Calculated cell parameters (using the TOPAS program [30]) for representative $Mn_{3-x}Mg_xFe_4(PO_4)_6$ powdered samples (1000 °C-fired).

Sample	Cell parameters and cell volume of the $Mn_{3-x}Mg_xFe_4(PO_4)_6$ major phase[a]						
	a (Å)	b (Å)	c (Å)	α	β	γ	V (Å^3)
$x = 0.0$	6.3660 (3)	8.0906 (3)	9.3232 (5)	105.219 (4)	108.116 (4)	102.045 (4)	41,774 (4)
$x = 0.5$	6.3578 (3)	8.0724 (3)	9.3166 (5)	105.139 (3)	108.118 (4)	101.957 (4)	41,644 (4)
$x = 1.0$	6.3485 (2)	8.0443 (4)	9.3058 (5)	105.046 (4)	108.125 (4)	101.827 (4)	41,450 (4)
$x = 1.5$	6.3414 (2)	8.0182 (4)	9.2983 (4)	104.928 (3)	108.162 (3)	101.695 (4)	41,293 (3)
$x = 2.0$	6.3396 (3)	7.9945 (4)	9.2938 (4)	104.894 (4)	108.205 (4)	101.619 (5)	41,155 (4)
$x = 2.5$	6.3318 (3)	7.9621 (4)	9.2816 (5)	104.794 (4)	108.265 (4)	101.475 (4)	40,931 (4)
$x = 3.0$	6.3264 (3)	7.9229 (5)	9.2682 (5)	104.689 (4)	108.390 (5)	101.331 (5)	40,662 (4)

[a] The formed phosphate solid solutions should be more appropriately written as $(Mn,Mg)_{3-y}Fe_{4+z}(PO_4)_6$ since there is a defect of Mg (Mn + Mg < 3) and an excess of Fe (>4), according to the presence of secondary phases of Mg.

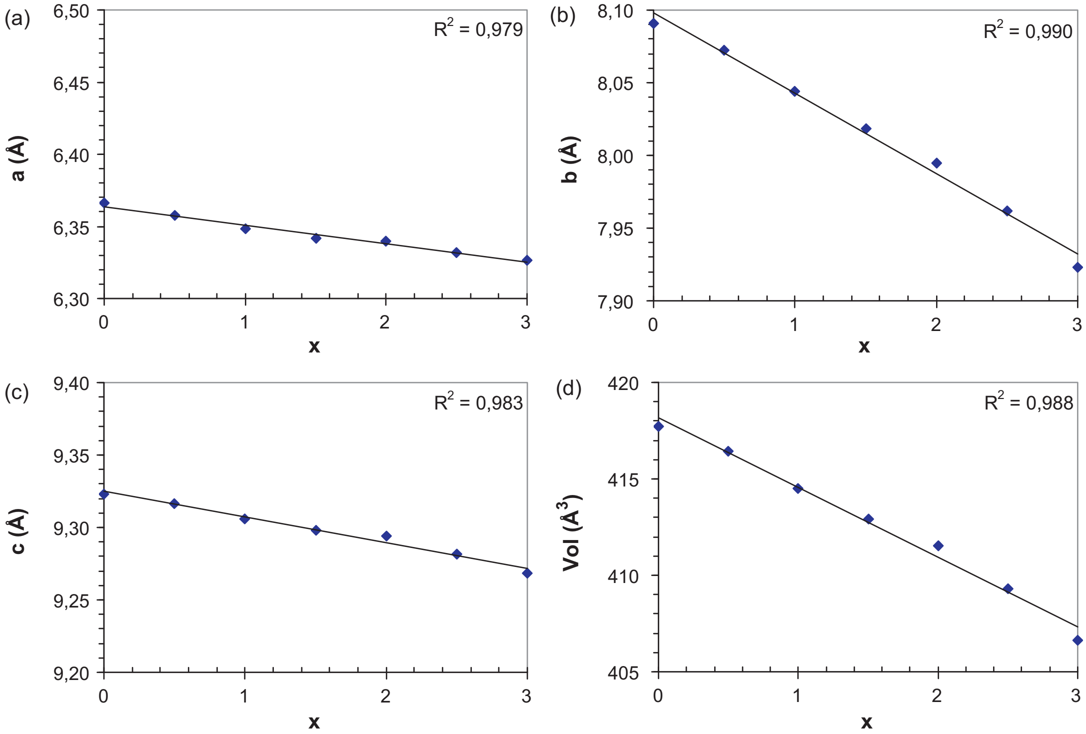

Fig. 4. Evolution of cell parameters *a*, *b* and *c* (*a–c*), and cell volume (*d*) with Mg doping (*x*) for representative $Mn_{3-x}Mg_xFe_4(PO_4)_6$ phosphate samples (*x* = 0, 0.5, 1.0, 1.5, 2.0, 2.5 and 3.0) fired at 1000 °C/4 h (obtained from the TOPAS fitting [30]).

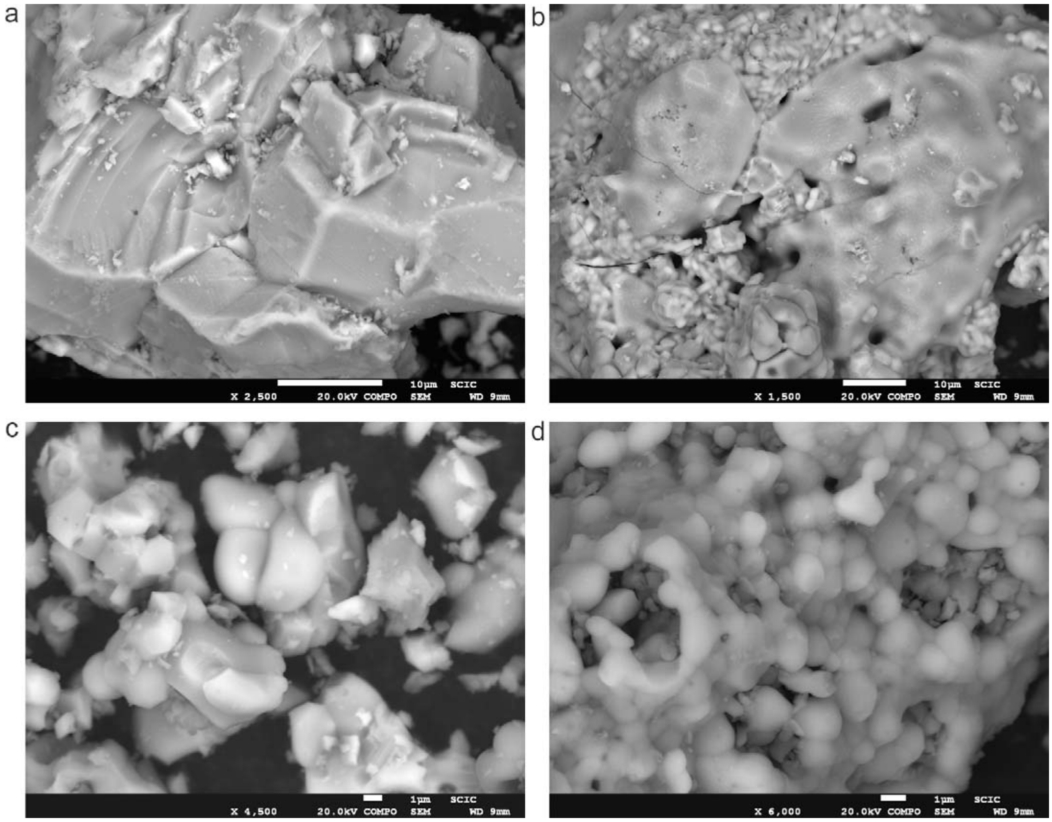

Fig. 5. Representative SEM images corresponding to selected 1000 °C-fired samples: (a) D1 (*x* = 0; $Mn_3Fe_4P_6O_{24}$), (b) D3 (*x* = 1; $Mn_2Mg_1Fe_4P_6O_{24}$), (c) D5 (*x* = 2; $Mn_1Mg_2Fe_4P_6O_{24}$) and (d) D7 (*x* = 3; $Mg_3Fe_4P_6O_{24}$).

bipyramid) [19,23]. Remarkably, it may be also appreciated that the *b*-axis diminishes about 3 or 4 times more than *a*- and *c*-axis, which is indicative of a considerable anisotropy in the unit cell variation. This anisotropy could be due to the preferential entrance of Mg ions into some of the cationic sites. However, a more complete structural study of the occupancy of the four different cationic sites (M(1)–M(4)) by the bivalent (Mn and Mg) and trivalent (Fe) cations has not been carried out, since it was out of the scope of the present study.

3.3. Electron microscopy characterization (SEM/EDX)

To gain further information about the morphology, homogeneity and composition of the samples at the microscale, SEM/EDX characterization was performed with selected fired samples. Representative SEM images of selected $Mn_{3-x}Mg_xFe_4(PO_4)_6$ compositions (D1, D3, D5 and D7) calcined at 1000 °C may be appreciated in Fig. 5. In general terms, the morphology of samples is quite homogeneous and consists of partially sintered and monolithic aggregates (specially D1 sample) having large sizes (several tens of μm), which in turn are constituted by smaller round-grained particles (1–5 μm).

To better characterize the chemical composition and homogeneity of the samples, EDX analyses were performed in different regions of the samples (a minimum of 6 analyses per sample). Representative EDX analyses of selected samples (D1, D3, D5 and D7) are shown in Fig. 6 (they correspond to the regions shown in the SEM images in Fig. 5). The analyses showed that the samples were quite homogeneous, specially for $x < 2$ (D1–D4 samples), obtaining only a slight dispersion in the molar Mn:Mg:Fe:P ratios through the different analyzed regions. For samples with $x \geq 2$ (D5–D7), there were also some aggregate regions where the EDX analyses (not shown for brevity reasons) indicated the predominance of Mg and P elements, with Mn and Fe having very weak intensity signals. Thus, these aggregates would correspond to regions enriched in β-$Mg_2P_2O_7$ diphosphate (or also α-$Mg_2P_2O_7$ for D7), which was more abundant in these samples (D5–D7) according to XRD characterization.

The theoretical and experimental (EDX-measured) average compositions of selected samples are summarized in Table 4. The shown semiquantitative average compositions are representative of solid solution aggregates (specially for samples D5 and D7), after discarding the analyses performed in Mg-enriched regions (due to the presence of β-$Mg_2P_2O_7$ and/or α-$Mg_2P_2O_7$ crystals). As it may be observed the experimental compositions are quite close to the theoretical initial formulations, although with a slight excess of Fe (>4) with respect to the sum of Mn + Mg (<3). This is in accordance with the presence of $(Mn,Mg)_{3-y}Fe_{4+z}(PO_4)_6$ solid solution aggregates with compositions related to that of the already known

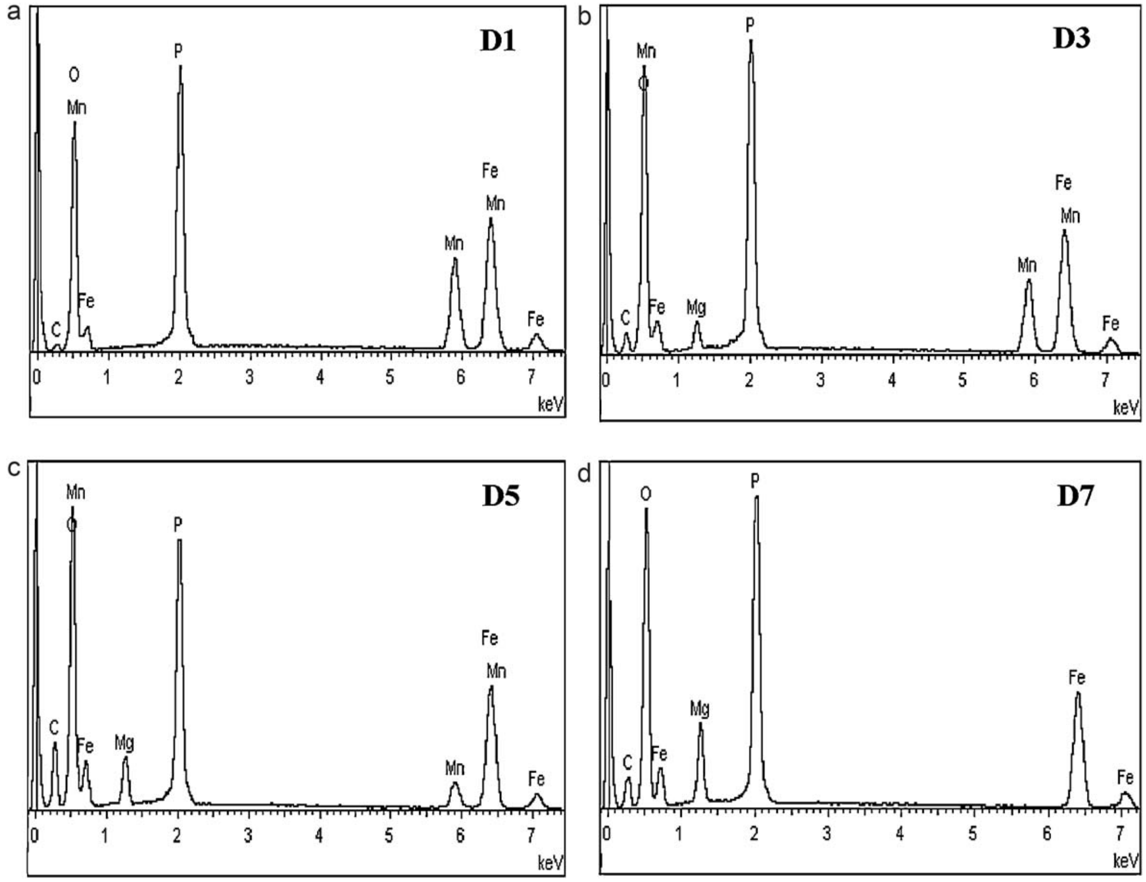

Fig. 6. Representative EDX analyses of selected 1000 °C-fired samples (correspond to the regions shown in the SEM images in Fig. 5): (a) D1 ($x = 0$; $Mn_3Fe_4P_6O_{24}$), (b) D3 ($x = 1$; $Mn_2Mg_1Fe_4P_6O_{24}$), (c) D5 ($x = 2$; $Mn_1Mg_2Fe_4P_6O_{24}$) and (d) D7 ($x = 3$; $Mg_3Fe_4P_6O_{24}$).

Table 4
Theoretical (initial) formulations and the corresponding EDX-measured average compositions for selected $Mn_{3-x}Mg_xFe_4(PO_4)_6$ samples (1000 °C-fired powders).

Sample	Theoretical formulation	Average EDX composition (atomic)[a]			
		Mn	Mg	Fe	P
D1 ($x = 0$)	$Mn_3Fe_4(PO_4)_6$	3.0 (2)	–	4.2 (6)	6.0 (5)
D3 ($x = 1$)	$Mn_2Mg_1Fe_4(PO_4)_6$	1.9 (3)	0.94 (7)	4.1 (6)	6.0 (6)
D5 ($x = 2$)	$Mn_1Mg_2Fe_4(PO_4)_6$	1.0 (1)	1.7 (3)	4.4 (6)	6.0 (5)
D7 ($x = 3$)	$Mg_3Fe_4(PO_4)_6$	–	2.7 (3)	4.2 (4)	6.0 (3)

[a] The compositions have been normalized to 6 mol of P. The standard deviation (of the last figure) is shown between brackets.

$Mn_{2.06}Fe_{4.94}(PO_4)_6$ compound, along with secondary phases containing Mn and Mg ($Mn_2P_4O_{12}$, and β-$Mg_2P_2O_7$ and α-$Mg_2P_2O_7$ diphosphates).

3.4. UV–vis–NIR spectroscopy and colour characterization

The UV–vis–NIR spectra of selected 1000 °C-fired powders (above) and of the corresponding enamelled samples (below) are shown in Fig. 7. Regarding to the spectra of $Mn_{3-x}Mg_xFe_4(PO_4)_6$ fired powders (D1, D3, D5 and D7), the observed absorptions are mainly characteristic of Fe(III) and Mn(II) ions (both having a d^5 configuration) in an octahedral coordination environment (cationic sites M(1), M(2) and M(4) in the $(Mn,Mg)^{II}_{3-}Fe^{III}_4(XO_4)_6$ structure), with a negligible contribution of Mn(II) ions in trigonal bipyramid coordination (M(3) cationic site). [34] Thus, the absorptions around 961–1000 nm, 605–690 nm, and 432–522 nm could be associated, respectively, to the ν_1 ($^6A_1(^6S) \rightarrow {}^4T_1(^4G)$), ν_2 ($^6A_1(^6S) \rightarrow {}^4T_2(^4G)$) and ν_3 (degenerate $^6A_1(^6S) \rightarrow {}^4E,{}^4A_1(^4G)$) transitions of octahedral Fe(III) and Mn(II) [35,36]. Moreover, there is a charge transfer band in the UV region at around 320–334 nm. Noteworthy, all the absorptions broaden or extend to higher wavelengths (or lower energies) with the increase of the amount of Mn in the fired $Mn_{3-x}Mg_xFe_4(PO_4)_6$ samples (lower Mg doping, x): for instance, the absorptions observed at *ca.* 432, 605 and 961 nm for D7 sample ($x = 3$, $Mg_3Fe_4(PO_4)_6$) are broadened progressively up to *ca.* 522, 690 and 1000 nm for D1 sample ($x = 0$, $Mn_3Fe_4(PO_4)_6$), respectively, due to the additional bands of Mn(II). These additional bands of Mn(II) occur at lower energies (higher wavelengths), explaining the observed broadening of the bands, and this fact is in accordance with the lower value of Dq for Mn(II) than for analogous Fe(III) systems [35].

As a result of these absorptions, the $Mn_{3-x}Mg_xFe_4(PO_4)_6$ fired powders (1000 °C) exhibited yellowish colourations up to $x = 1.5$ and yellowish-green colourations for $x \geq 2$ (see the values of the colourimetric $L^*a^*b^*$ parameters in Table 5, left). As it may be appreciated, the yellow component (positive b^* value) increases with Mg doping up to $x = 1.5$, and then decreases for $x > 1.5$, while the green component (negative a^*) becomes noticeable for $x \geq 2$. Also remarkably, the colour of the fired powders becomes lighter (or less intense; higher L^* value) with the increase of Mg doping (x).

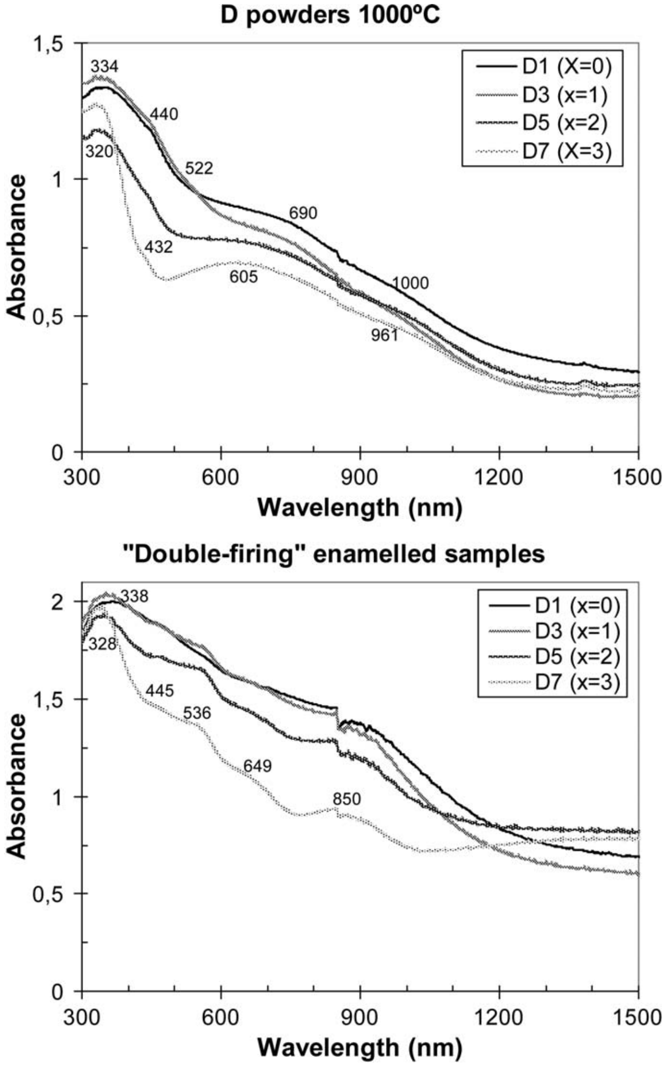

Fig. 7. UV–vis–NIR spectra of selected $Mn_{3-x}Mg_xFe_4(PO_4)_6$ samples (D1, D3, D5 and D7): 1000 °C-fired powders (above), and powders enamelled within the double-firing glaze (below).

In order to test the colouring performance of the samples as potential ceramic dyes, the 1000 °C-fired powders were enamelled within a conventional (double-firing) transparent ceramic glaze. Remarkably, the obtained enamelled samples exhibited all of them an interesting and similar dark-brown colouration, irrespective of the amount of Mg doping (x) in the formulation (see the aspect of selected enamelled samples in Fig. 8). Moreover, it was observed a favourable reduction of the typical ‘‘pin-hole’’ degasification defect with the increase of Mg doping in the formulation. If we consider that the relative amount of Mn and Mg in the sample has a negligible effect on the final colour of enamelled samples, thus, the similar colour developed in all cases could be associated to the similar amount of Fe present in all of them, as it will be analyzed in detail in next section. As it may be appreciated in Table 5, all the samples exhibit low and positive a^* (2.8–5.3) and b^* (4.3–8.3) values, and also very low L^* values (18.6–27.69), typical of intense (highly saturated) dark-brown colourations. The corresponding UV–vis–NIR spectra of selected enamelled samples are shown in Fig. 7. Apart from the typical charge transfer band at around 328–338 nm, all the spectra exhibit the same main absorptions centred at around 445–536, 649 and

Table 5
Colour parameters (CIE-$L^*a^*b^*$) of $Mn_{3-x}Mg_xFe_4(PO_4)_6$ fired powders (1000 °C) and of the corresponding enamelled samples (double-firing ceramic glaze).

1000 °C-fired powders				Enamelled samples			
Sample	L^*	a^*	b^*	Sample	L^*	a^*	b^*
D1 ($x = 0$)	50.0	−0.3	9.0	D1 ($x = 0$)	19.4	3.0	8.3
D2 ($x = 0.5$)	51.0	3.1	10.3	D2 ($x = 0.5$)	27.9	2.8	5.5
D3 ($x = 1$)	52.1	2.0	11.2	D3 ($x = 1$)	22.3	3.3	5.6
D4 ($x = 1.5$)	57.4	1.3	14.1	D4 ($x = 1.5$)	20.1	3.1	6.5
D5 ($x = 2$)	57.0	−2.3	8.0	D5 ($x = 2$)	18.6	4.0	4.3
D6 ($x = 2.5$)	60.3	−3.0	7.1	D6 ($x = 2.5$)	20.1	5.2	5.8
D7 ($x = 3$)	62.7	−3.3	1.8	D7 ($x = 3$)	26.3	5.3	6.6

850 nm. These absorptions correlate quite well with those of Fe(III) in an octahedral coordination environment (with oxide ligands), as in hematite iron oxide (α-Fe_2O_3). Indeed, a typical absorption spectrum of reddish bulk hematite [37] usually presents an intense charge transfer band centred at 290 nm due to iron–ligands interaction, followed by a band at 850 nm and two shoulders at 600–660 and 480–580 nm, that are attributed respectively to the spin-forbidden $^6A_1 \rightarrow {}^4T_1$ (ν_1), $^6A_1 \rightarrow {}^4T_2$ (ν_2), and $^6A_1 \rightarrow {}^4E,{}^4A_1$ (ν_3) transitions of Fe^{3+} in octahedral environment (corundum structure of hematite). Therefore, these absorption bands would be in accordance with the existence of iron oxide in enamelled samples as a consequence of some interaction between the Fe-rich solid solution and the double-firing ceramic glaze, as it will be discussed in next section.

Accordingly, the obtained solid solutions (1000 °C-fired) with a minimized Mn content (specially the $Mg_3Fe_4(PO_4)_6$ formulation, without Mn) could be used as low-toxicity Fe reservoirs for conferring an intense dark-brown colouration to conventional double-firing ceramic glazes. They could be a less hazardous alternative to other classical or less conventional brown ceramic pigments. Indeed, most of the classical brown ceramic pigments are based on rutile and spinel structures containing hazardous elements such as Cr, Ni, Zn or Sb (i.e. ceramic pigments with DCMA [38] classification numbers 11-46-7, 13-33-7, 13-35-7 and 13-51-7). The recently developed karrooite-based ($MgTi_2O_5$ doped with Fe and Mn) [39] and srilankite-based ($ZrTiO_4$ doped with Fe and Mn) [40] brown ceramic pigments would be less hazardous alternatives. Similarly, the orthophosphate formulations herein prepared would only involve the use of Fe (and optionally some Mn) as heavy metal, being thus a lower-toxicity alternative to the conventional brown ceramic pigments containing hazardous transition metals.

3.5. Interaction of solid solution fired powders with the double-firing ceramic glaze

Since the colour of fired powders (yellowish green) and enamelled samples (dark brown) was quite different, some interaction or reaction between the solid solution particles and the glassy matrix of the ceramic glaze must have occurred during the enamel firing (at a maximum temperature of 1000 °C). This possible interaction was analyzed by performing SEM–EDX and XRD (grazing-angle) analyses onto the surface of enamelled samples. Fig. 9a shows a general SEM overview (at a low magnification) of the surface of a selected enamelled sample (D5), obtained with the electron back-scattering detector. The presence of many white and darker (grey) spots (10–30 μm) with rounded morphologies may be appreciated, embedded in the dark glassy matrix. This dark glassy matrix may be better appreciated in the SEM image shown in Fig. 9b (obtained at a higher magnification) and appears to be composed by two different phases: a darker region (1) and white-grey morphologies (2). The EDX analysis of the darker phase (region 1) may be observed in Fig. 9c and corresponds to the typical spectrum of the ceramic glaze (SiO_2–Al_2O_3–PbO–CaO–Na_2O–K_2O system), although with a

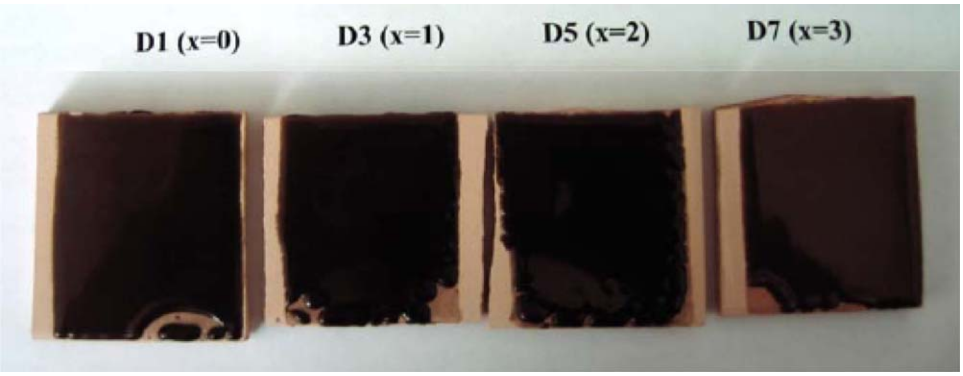

Fig. 8. Aspect of representative $Mn_{3-x}Mg_xFe_4(PO_4)_6$ enamelled samples (within the double-firing ceramic glaze). (For interpretation of the references to colour in this figure legend, the reader is referred to the web version of the article.)

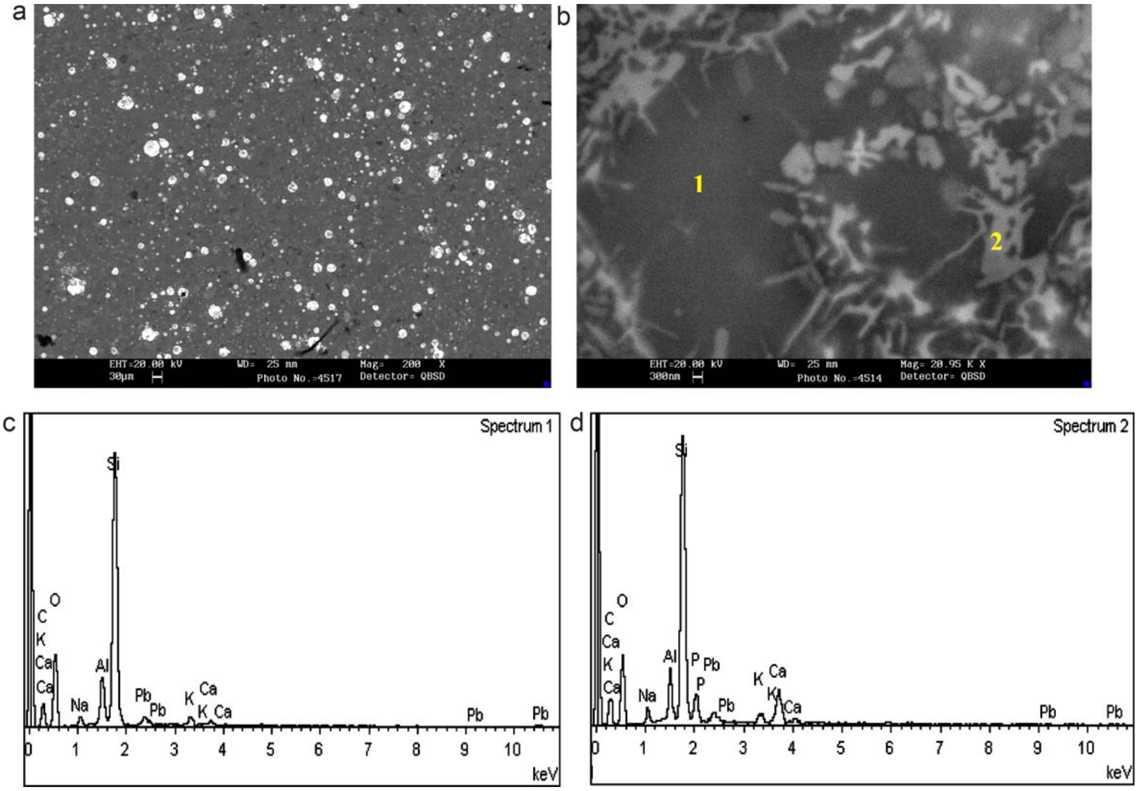

Fig. 9. Representative SEM images (general view at low magnification, a, and detail of the glassy phase, b) and EDX analyses (c and d) of sample D5 (local regions labelled as 1 and 2 in b) enamelled within the double-firing glaze.

reduced amount of Pb and Ca with respect to the parent (original) ceramic glaze (EDX not shown for brevity reasons). On the other hand, the EDX analysis (Fig. 9d) of the small ($<$1–2 μm) grey morphologies (phase or region 2) is very similar to the previous spectrum of the darker region, although the signal of Ca is considerably more intense, and it contains also some P which must have segregated from the solid solution particles. EDX peaks of the metals present in the solid solution (Mn, Mg or Fe) are not observed in both analyses. Therefore, this dark glassy matrix composed of two different regions (one of them enriched in Ca and P elements) cannot be responsible for the dark-brown colour of enamelled samples, and thus this colour must be associated to the round white (or grey) spots observed at a lower magnification (Fig. 9a).

In this respect, Fig. 10a shows the SEM image of one of these abundant white spots (present in all enamelled samples) at a higher magnification (we have selected D1 sample). As it may be appreciated, it is composed by different phases (regions labelled as 1–3). The corresponding EDX analyses (Fig. 10b–d) confirm that some reaction has occurred between the dispersed $Mn_{3-x}Mg_xFe_4(PO_4)_6$ solid solution particles and the Pb- and Ca-containing ceramic glaze. On the one hand, the EDX spectra of the whiter (1) and grey (3) regions are quite similar and confirm this reaction, since the EDX spectra contain the peaks (strong intensity) of the elements present in the D1 solid solution (P, Mn and Fe) and also very intense peaks associated to Pb and Ca coming from the ceramic glaze. Therefore, Pb and Ca segregate to a large extent from the ceramic glaze to react (and associate) with the disperse solid solution particles, originating the whiter (region 1; more Pb and Fe-enriched) and grey phases (region 2; with less Pb, more Mn and less Fe). These phases are phosphate-enriched regions containing Pb, Ca, Mn, Mg (for $x > 0$) and Fe elements. On the other hand, the darker phase also present in the white spots (region 2) exhibits an EDX spectrum which is characteristic of iron oxide (with residual traces of Mn). Therefore, in the reaction of the disperse solid solution particles with the ceramic glaze, considerable amounts of Fe also segregate or abandon the original solid solution to be stabilized in the ceramic glaze as iron oxide particles. EDX analyses performed (Fig. 10f) onto other darker spots present in the ceramic glaze (region 4 in the SEM image shown in Fig. 10e), also indicate the formation of calcium (and Mn) phosphate-enriched regions (4) as a consequence of the interaction between the ceramic glaze and the solid solution particles during the enamel firing.

Finally, grazing-angle XRD measurements were performed onto selected enamelled samples (D1, D5 and D7) to detect the possible presence of crystalline phases. In all the measured samples the XRD patterns presented the same features. A representative XRD spectrum (sample D7) is shown in Fig. 11. Apart from the characteristic amorphous halo (of a SiO_2-containing glassy phase) between 20 and 25° 2θ, other weak intensity peaks corresponding to some crystalline phases were detected: these phases were $Na_2Al_2Si_5O_{14}$ (labelled as N; PDF number 048-0733 and main XRD peak centred at around 26.6° 2θ), $Na_{1.84}Al_2Si_{2.88}O_{9.68}$ (labelled as N′; PDF number 048-0731 and main XRD peak centred at around 31.1° 2θ), β-$Ca_3(PO_4)_2$ (labelled as C; PDF number 070-2065 and main XRD peak

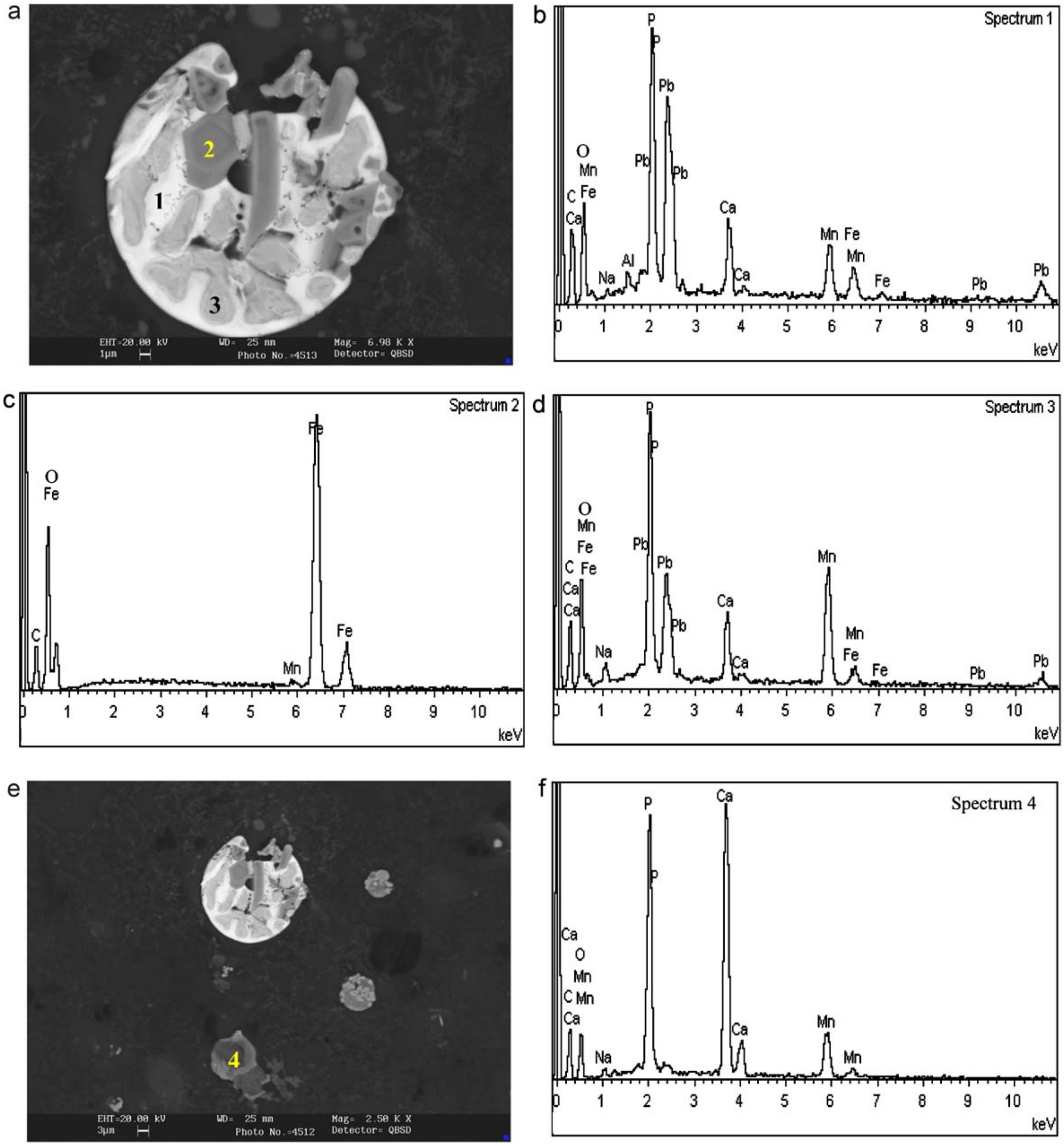

Fig. 10. Representative SEM images (a and e) and EDX analyses (b–d and f) of sample D1 (local regions labelled as 1–4) enamelled within the double-firing glaze.

centred at around 31.0° 2θ) and hematite α-Fe_2O_3 (labelled as H; PDF number 033-0664 and main XRD peak centred at around 33.2° 2θ). The presence of crystalline hematite and β-$Ca_3(PO_4)_2$ particles is in accordance with the previous SEM–EDX characterization (darker particles observed in regions 2 and 4 in Fig. 10a and e, with the corresponding EDX analyses in Fig. 10c and f). Moreover, the presence of iron oxide hematite particles would also explain the UV–vis absorption bands observed in enamelled samples. However, none crystalline phase of any phosphate of Pb, Ca, Mn, Mg and/or Fe was detected (therefore, regions 1 and 3 observed in Fig. 10a must be rather amorphous). Accordingly, the similar and intense dark-brown colourations exhibited by all the enamelled samples, irrespective of the Mn content (or Mg doping), appears to be mostly due to hematite particles stabilized in the ceramic glaze, and presumably also due to the Fe solubilized in the amorphous phosphate-enriched regions containing also Pb, Ca, Mn and Mg (regions 1 and 3 in Fig. 10a).

Despite of the fact that the prepared solid solutions are not stable enough and react with the double-firing ceramic glaze, we must remark that this reaction results in the favourable stabilization of hematite iron oxide particles within the glassy matrix. Thus, the obtained orthophosphate solid solutions can act as pigment additives, obtained by converting most of their iron content into hematite, which mainly confers the ceramic glaze a nice and intense dark-brown colouration. A similar effect was observed when using Fe-containing granite sawing wastes (GSW) for the production of coloured cement-based mortars [41]. We must highlight that this stabilization of α-Fe_2O_3 in a ceramic glaze cannot be easily accomplished when using any other iron salt or even directly Fe_2O_3 as iron precursors, since Fe becomes mostly solubilized in the glassy

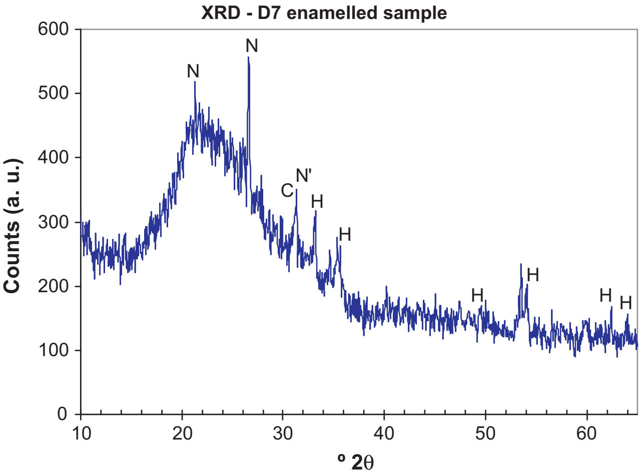

Fig. 11. XRD pattern (grazing-angle) of a selected sample (D7, $x = 3$) enamelled within the double-firing glaze. *Crystalline phases: H* = hematite (α-Fe_2O_3), $N = Na_2Al_2Si_5O_{14}$, $N' = (Na_{1.84}Al_2Si_{2.88}O_{9.68})$ and $C = \beta$-$Ca_3(PO_4)_2$.

matrix producing generally orange, reddish or pale-brown colourations, with an important lack of reproducibility. Indeed, to avoid the solubilization of Fe into ceramic glazes some heteromorphic pigments have been developed which are based on the encapsulation of the colouring hematite particles into protecting crystals (such as SiO_2 or $ZrSiO_4$ crystals) [37,42,43]. However, these encapsulation processes are not simple to accomplish and also lack of some reproducibility.

4. Conclusions

Solid solutions of mixed metal $Mn_{3-x}Mg_xFe_4(PO_4)_6$ orthophosphates ($x = 0, 0.5, 1, 1.5, 2, 2.5$, and 3) were prepared for the first time (from coprecipitate powders calcined at 1000 °C/4 h), and they were characterized by thermal analysis, XRD, SEM/EDX, UV–vis–NIR spectroscopy and colour measurements (CIE-$L^*a^*b^*$). Relatively homogeneous orthophosphate $(Mn,Mg)_{3-y}Fe_{4+z}(PO_4)_6$ solid solutions having the $Fe_7(PO_4)_6$ structure type formed successfully as the major crystalline phase within the studied range of compositions, accompanied only by variable quantities of α- and/or β-$Mg_2P_2O_7$ diphosphates as secondary phases (also residual $Mn_2P_4O_{12}$ for $x = 0$).

Interestingly, the obtained solid solutions (1000 °C-fired) were tested as potential ceramic dyes for the colouration of double-firing ceramic glazes, and they produced nice and intense dark brown colourations. Moreover, the obtained colourations were very similar in all samples, irrespective of the different amount of Mn (or Mg) in the formulations. This was explained by the occurrence of a reaction between the disperse solid solution particles and the double-firing ceramic glaze upon the enamel firing: remarkably, considerable amounts of Fe segregated from the solid solutions to be stabilized as hematite (α-Fe_2O_3) particles in the ceramic glaze, and being the main responsible for the intense dark-brown colourations. Thus, the obtained solid solutions having a minimized Mn content (especially $Mg_3Fe_4(PO_4)_6$ composition) could serve as low-toxicity Fe reservoirs to stabilize hematite in double-firing glazes and produce an interesting dark-brown colouration, being an alternative to other brown ceramic pigments containing hazardous metals (i.e. Cr, Ni, Zn, or Sb).

Acknowledgements

The authors thank the Spanish "*Ministerio de Educación y Ciencia*" (project MAT2008-02893) for financial support. Moreover, the technical assistance provided by the Central Services of Scientific Instrumentation (SCIC) of the University Jaume I is also fully acknowledged.

References

[1] H. Onoda, K. Yokouchi, K. Kojima, H. Nariai, Addition of rare earth cation on formation and properties of various cobalt phosphates, Mater. Sci. Eng. B 116 (2005) 189–195.
[2] H. Onoda, H. Matsui, I. Tanaka, Improvement of acid and base resistance of nickel phosphate pigment by the addition of lanthanum cation, Mater. Sci. Eng. B 141 (2007) 28–33.
[3] S. Meseguer, M.A. Tena, C. Gargori, J.A. Badenes, M. Llusar, G. Monrós, Structure and colour of cobalt ceramic pigments from phosphates, Ceram. Int. 33 (2007) 843–849.
[4] S. Meseguer, M.A. Tena, C. Gargori, R. Galindo, J.A. Badenes, M. Llusar, G. Monrós, Development of blue ceramic dyes from cobalt phosphates, Ceram. Int. 34 (2008) 1431–1438.
[5] V. Buissete, D. Giaume, T. Gacoin, J.P. Boilot, Aqueous routes to lanthanide-doped oxide nanophosphors, J. Mater. Chem. 16 (2006) 529–539.
[6] H. Onoda, H. Nariai, A. Moriwaki, I. Motooka, Formation and catalytic characterization of various rare earth phosphates, J. Mater. Chem. 12 (2002) 1754–1760.
[7] C. Pan, S. Yuan, W. Zhang, A neutral templating route to mesoporous titanium phosphate molecular sieves with enhanced thermal resistance, Appl. Catal. A 312 (2006) 186–193.
[8] D. Chandra, N. Kishor, A. Bhaumik, Novel silicontinphosphate molecular sieve with high anion exchange capacity, J. Mol. Cat. A 247 (2006) 216–221.
[9] W.H.J. Hogarth, J.C. Diniz da Costa, J. Drennan, C.Q. Max Lu, Proton conductivity of mesoporous sol–gel zirconium phosphates for fuel cell applications, J. Mater. Chem. 15 (2005) 754–758.
[10] X. Zhang, J.Q. Xu, J.H. Yu, J. Lu, Y. Xu, Y. Chen, T.G. Wang, X.Y. Yu, Q.F. Yang, Q. Hou, Structural characterizations and magnetic properties of three new reduced molybdenum phosphates, J. Solid State Chem. 180 (2007) 1949–1956.
[11] M. Vallet-Regi, Revisiting ceramics for medical applications, Dalton Trans. (2006) 5211–5220.
[12] M. Fores, J.A. Llusar, J. Badenes, M.A. Calbo, G. Tena, Monrós, Cobalt minimisation in willemite ($Co_xZn_{2-x}SiO4$) ceramic pigments, Green Chem. 2 (2000) 93–100.
[13] A. García, M. Llusar, J. Calbo, M.A. Tena, G. Monrós, Low-toxicity red ceramic pigments for porcelainised stoneware from lanthanide-ceria solid solutions, Green Chem. 3 (2001) 238–242.
[14] M. Jansen, H.P. Letschert, Inorganic yellow-red pigments without toxic metals, Nature 404 (2000) 980–982.
[15] S. Furukawa, T. Masui, N. Imanaka, Synthesis of new environmentally friendly yellow pigments, J. Alloys Comp. 418 (2006) 255–258.
[16] M. LLusar, A. Zielinska, M.A. Tena, J.A. Badenes, G. Monrós, Blue-violet ceramic pigments based on Co and Mg $Co_{2-x}Mg_xP_2O_7$ diphosphates, J. Eur. Ceram. Soc. 30 (2010) 1887–1896.
[17] P. Lightfoot, A.K. Cheetman, Neutron-diffraction study of the cation distributions in the systems $Fe_{7-x}M_x(PO_4)_6$ (M = Mn or Co), J. Chem. Soc. Dalton Trans. (1989) 1765–1769.

[18] R. Glaum, Thermal-behavior of anydrous phosphates. 8. Synthesis and crystal-structure of $Cr_7(PO_4)_6$ – 1st mixed-valence phosphate with Cr(II) and Cr(III), Z. Kristallogr. 205 (1993) 69–83.

[19] M. Gruss, R. Glaum, Preparation and single crystal structure refinement of mixed orthophosphates $M_3Cr_4(PO_4)_6$ (M = Mg, Zn, Cu) – copper(II) in compressed octahedral coordination, Z. Kristallogr. 212 (1997) 510–518.

[20] A.A. Belik, A.P. Malakho, K.V. Pokholok, B.I. Lazoryak, X-ray powder diffraction, Mossbauer spectroscopy, and thermal stability of $Fe_7(PO4)_6$, Russ. J. Inorg. Chem. 44 (1999) 1457–1464.

[21] A.A. Belik, K.V. Pokholok, A.P. Malakho, S.S. Khasanov, B.I. Lazoryak, Synthesis and structure of phosphates $M_3R_4(PO4)_6$ (M = Cu, Co; R = Fe, Cr, Ga, In) and their interaction with hydrogen, Russ. J. Inorg. Chem. 45 (2000) 1494–1509.

[22] Y.A. Gorbunov, B.A. Maksimov, Y.K. Kabalov, A.N. Ivashchenko, O.K. Mel'nikov, N.V. Belov, The crystal structure of $Fe_3Fe_4(PO_4)_6$, Dokl. Akad. Nauk. SSSR 254 (1980) 873–877.

[23] A.A. Belik, A.P. Malakho, K.V. Pokholok, B.I. Lazoryak, S.S. Khasanov, New mixed-valent iron (II/III) phosphates, $Cu_{3-x}Fe_{4+x}(PO_4)_6$, J. Solid State Chem. 150 (2000) 159–166.

[24] A. Bezkrovnyi, N. Guskos, J. Typek, N.Y. Ryabova, M. Bosacka, A. Blonska-Tabero, M. Kurzawa, I. Rychlowska-Himmel, G. Zolnierkiewicz, Neutron diffraction study of $Mn_3Fe_4V_6O_{24}$, Mater. Sci. (Poland) 23 (2005) 884–889.

[25] A. Bezkrovnyi, N. Guskos, J. Typek, N.Y. Ryabova, A. Blonska-Tabero, G. Zolnierkiewicz, Crystal structure of $Mg_3Fe_4V_6O_{24}$ studied by neutron diffraction, Rev. Adv. Mater. Sci. (2006) 166–171.

[26] G. Zolnierkiewicz, N. Guskos, J. Typek, E.A. Anagnostakis, A. Blonska-Tabero, M. Bosacka, Competition of magnetic interactions in $M_3Fe_4V_6O_{24}$ (M(II) = Zn, Cu, Mn, Mg) compounds studied by EPR, J. Alloys Compd. 471 (2009) 28–32.

[27] M. Weil, $Fe^{II}{}_3Fe^{III}{}_4(AsO_4)_6$, the first arsenate adopting the $Fe_7(PO_4)_6$ structure type, Acta Crystallogr. E 60 (2004) i139–i141.

[28] C. Gicquel-Mayer, M. Mayer, G. Pérez, Structural study of silver and zinc bimolybdate $Ag_2Zn_2Mo_3O_{12}$, Acta Crystallogr. B 37 (1981) 1035–1039.

[29] European Decision 2000/532/CE of 3 May 2000 (Official Journal of the European Communities, L 226, 6.9.2000, p. 3-24) adopting the European Waste Catalogue (EWC).

[30] A.X.S. Bruker, TOPAS V2. 1. General Profile and Structure Analysis Software for Powder Diffraction Data, User's Manual, A.X.S. Bruker, Karlsruhe, Germany, 2003.

[31] R.W. Cheary, A.A. Coelho, A fundamental parameters approach to X-ray line-profile fitting, J. Appl. Crystallogr. 25 (1992) 109–121.

[32] CIE, Recommendations on uniform colour spaces, colour difference equations, psychometrics colour terms, in: Suplement n 2 of CIE Publ. N 15 (E1-1. 31) 1971, Bureau Central de la CIE, Paris, 1978 .

[33] R.D. Shannon, Revised effective ionic radii and systematic studies of interatomic distances in halides and chalcogenides, Acta Crystallogr. A32 (1976) 751–767.

[34] M. Ciampolini, C. Mengozzi, Quartet levels and spectra of 5-coordinate manganese(II) complexes, Gazz. Chim. Ital. 104 (1974) 1059–1066.

[35] A.B.P. Lever, Inorganic Electronic Spectroscopy, second ed., Elsevier Science B.V, The Netherlands, 1977, pp. 507–511.

[36] M. Dondi, G. Cruciani, G. Guarini, F. Matteucci, M. Raimondo, The role of counterions (Mo, Nb, Sb, W) in Cr-, Mn-, Ni- and V-doped rutiles ceramic pigments part 2. Colour and technological properties, Ceram. Int. 32 (2006) 393–405.

[37] A. García, M. Llusar, J. Badenes, M.A. Tena, G. Monrós, Encapsulation of hematite in zircon by microemulsion and sol–gel methods, J. Sol–Gel Sci. Technol. 27 (2003) 267–275.

[38] DCMA, Classification and Chemical Description of the Mixed Metal Oxide Inorganic Coloured Pigments, second ed., Dry color Manufacturer Association, Washington, DC, 1982.

[39] F. Matteucci, G. Cruciani, M. Dondi, G. Gasparoto, D.M. Tobaldi, Crystal structure, optical properties and colouring performance of karrooite $MgTi_2O_5$ ceramic pigments, J. Solid State Chem. 180 (2007) 3196–3210.

[40] M. Dondi, F. Matteucci, G. Cruciani, Zirconium titanate ceramic pigments: crystal structure, optical spectroscopy and technological properties, J. Solid State Chem. 179 (2006) 233–246.

[41] I. Mármol, P. Ballester, S. Cerro, G. Monrós, J. Morales, L. Sánchez, Use of granite sawing wastes for the production of coloured cement-based mortars, Cement Concrete Comp. 32 (2010) 617–622.

[42] J.B. Vicent, M. Llusar, J. Badenes, M.A. Tena, M. Vicente, G. Monrós, Occlusion of chromophore oxides by sol–gel methods: application to the synthesis of hematite–silica red pigments, Bol. Soc. Esp. Ceram. Vidr. 39 (2000) 83–93.

[43] M. Llusar, V. Royo, J.A. Badenes, M.A. Tena, G. Monrós, Nanocomposite Fe_2O_3–SiO_2 inclusion pigments from post-functionalized mesoporous silicas, J. Eur. Ceram. Soc. 29 (2009) 3319–3332.